

Reflected Iron Line From a Source Above a Kerr Black Hole Accretion Disc

Y. Dabrowski^{*} and A.N. Lasenby

Astrophysics Group, Cavendish Laboratory, Madingley Road, Cambridge, CB3 0HE, UK

Accepted ???. Received ???; in original form 26 April 2024

ABSTRACT

In this paper we present a fully relativistic approach to modelling both the continuum emission and the reflected fluorescent iron line from a primary X-ray source near a Kerr black hole. The X-ray source is located above an accretion disc orbiting around the black hole. The source is assumed to be a static point source located on an arbitrary position above the disc, on or off the axis of rotation. We carry out Monte Carlo simulations in order to estimate the iron line spectrum as well as its equivalent width. Because of the gravitational lensing effect, an enhancement of the iron line is expected when the primary source is located close to the central black hole. We find that for a source located on the axis of rotation the enhancement is relatively modest. An observer at inclination 30 degrees would measure an equivalent width of ~ 300 eV in the extreme case of a maximally rotating black hole and a source located at height 1.5 gravitational radius from the centre. This corresponds to an equivalent width enhancement factor of about 2 compared to the *classical* value where no lensing effect comes into play. However, when allowing the source to be located off the axis of rotation, much stronger enhancement can be obtained. In the extreme case of a maximally rotating black hole and a source located just above the approaching side of the disc, an observer at inclination 30 degrees could measure an equivalent width as high as ~ 1.5 keV (i.e. ~ 10 times the classical value). We also find that observers located at high inclination angles observe a stronger line than observers at low inclination angles.

Key words: accretion disks – black hole physics – line: profiles – X-rays: general

1 INTRODUCTION

It is now commonly agreed that Active Galactic Nuclei (AGN) are composed of a central supermassive black hole closely surrounded by a thin equatorial accretion disc, the emission process being controlled by viscous transport of angular momentum (see e.g. Rees 1984; Blandford and Rees 1992). The disc material is relatively *cold* ($\sim 10^6$ K) compared to the hard X-ray corona ($\sim 10^8$ K) by which it is surrounded. The corona is responsible for the observed X-ray continuum emission which follows a power-law of index $\Gamma \cong -1.7$. X-ray observation of Seyfert-1 galaxies revealed that there exist spectral features and other deviations from a simple power-law (e.g. Pounds et al. 1989; Nandra et al. 1989; Matsuoka et al. 1990). In particular a strong iron line is observed at 6.4 keV together with an excess in the continuum emission at energies higher than ~ 4 keV. This is well explained by Compton reflection re-processing of the hard X-ray power-law continuum onto the accretion disc (see e.g.

George & Fabian 1991; Matt, Perola & Piro 1991). The observed iron line is the result of fluorescent processes and the excess in the continuum is accounted for by the presence of a continuum component in the reflected emission. The detailed spectrum of the iron line is of great importance since it allows one to probe regions of the accretion disc as close as a few Schwarzschild radii from the central black hole (see e.g. Tanaka et al. 1995). In the particular case of MCG–6–30–15, the lineshape yields evidence that the emission occurs as close as half a Schwarzschild radius, giving strong support for the presence of a rotating Kerr black hole (Tanaka et al. 1995, Dabrowski et al. 1997).

The fluorescent iron line profile is well predicted by models which assume a power-law $\epsilon(r) \propto r^{-\alpha}$ for the fluorescent emissivity on the accretion disc, where $\alpha \sim 2$ (see e.g. Tanaka et al. 1995; Bromley, Chen & Miller 1997; Dabrowski et al. 1997; Reynolds & Begelman 1997; Cadez et al. 1998). In such cases the hard X-ray corona is assumed to be an extended source located above and below the disc so that approximately half of the emitted power illuminates the disc and is responsible for the reflected continuum component as

^{*} Email: youri@mrao.cam.ac.uk

well as observed fluorescent lines (George & Fabian 1991). The remaining half escapes to infinity and constitutes the major part of the observed continuum spectra. The predicted iron line equivalent width (EW) is in this case estimated to be $\sim 100 - 200$ eV (e.g. George & Fabian 1991, Matt et al. 1991). However, as discussed in Nandra et al. (1997), for a sample of 18 Seyfert-1 galaxies, observations reveal equivalent widths of 300-600 eV, or even as high as 1 keV in the case of MCG-6-30-15. Part of the EW enhancement may be explained by an overabundance of iron in the accretion disc material (e.g. Lee et al. 1998, 1999). However, other means of enhancement need to be found in order to account for large values of the iron line EW (Reynolds & Fabian 1997). Following the work of Martocchia & Matt (1996) and very recently Martocchia, Karas & Matt (1999), in this paper we propose to investigate the possible EW enhancement due to the gravitational lensing of the primary light rays which illuminate the disc and therefore drive the fluorescent process. The primary hard X-ray source is assumed to be a *static* point source located above the accretion disc. Situations where the source is located on or off the axis of rotation are both considered here.

Our predictions are based upon Monte Carlo simulations which account for the primary X-ray emission as well the reflected iron line in a consistent manner. It is assumed here that the primary continuum emission dominates over the reflected continuum emission so that the reflected continuum is neglected while calculating the line EW (see Section 4). Details of our fully relativistic theoretical approach are given in Section 2. Some results are given in the form of iron line profiles and equivalent widths in Section 3 for a primary source located on the axis of rotation. In Section 4, this assumption is relaxed and we investigate line profiles and equivalent widths for arbitrary positions of the source above the disc. Finally our results are discussed in Section 5.

2 REFLECTION MODEL IN THE KERR METRIC

The black holes considered here belong to the Kerr family of solutions to Einstein's equation and the metric employed is in the Boyer-Lindquist form, which is defined by

$$ds^2 = dt^2 - \rho^2 \left(\frac{dr^2}{\Delta} + d\theta^2 \right) - (r^2 + L^2) \sin^2 \theta d\phi^2 - \frac{2Mr}{\rho^2} (L \sin^2 \theta d\phi - dt)^2, \quad (1)$$

where

$$\rho^2 = r^2 + L^2 \cos^2 \theta, \quad (2)$$

$$\Delta = r^2 - 2Mr + L^2. \quad (3)$$

Here t , r , θ and ϕ are the space-time coordinates, M is the geometric mass, the mass of the black hole being Mc^2/G and the quantity LM is the angular momentum of the hole as measured at infinity (e.g. D'Inverno 1992). The gravity of the disc itself is assumed to be negligible and therefore the whole spacetime is described by the Boyer-Lindquist metric. We employ natural units $G = c = \hbar = 1$, unless stated otherwise.

2.1 Photon Path

Throughout this paper we use the gauge-theoretic formalism of Lasenby, Doran & Gull (1998) which allows fully relativistic and covariant calculations to be made in the context of an easy-to-handle flat space. It is important to note that predictions for measurable quantities agree *exactly* with those of General Relativity for this case. Equations relevant to an equivalent approach to the problem, but following a more standard general relativistic formalism, are presented in Appendix A.

The gauge-theoretic approach to gravity of Lasenby et al. (1998) employs the language of *geometric algebra*, which seems to most clearly expose the physics involved. In particular, the geometric algebra of spacetime (Hestenes 1966), known as the Space Time Algebra (STA), is generated by a set of four orthonormal vectors $\{\gamma_\mu\}$, $\mu = 0 \dots 3$, satisfying

$$\gamma_\mu \cdot \gamma_\nu = \eta_{\mu\nu} = \text{diag}(+ - - -). \quad (4)$$

In order to investigate problems in relation with the Kerr geometry, we also introduce a suitable set of coordinates t , r , θ and ϕ associated with the polar coordinate system and defined in terms of the fixed $\{\gamma_\mu\}$ frame. The corresponding coordinate frame $e_\mu \equiv \partial_\mu x$ is

$$e_t \equiv \gamma_0 \quad (5)$$

$$e_r \equiv \sin \theta \cos \phi \gamma_1 + \sin \theta \sin \phi \gamma_2 + \cos \theta \gamma_3 \quad (6)$$

$$e_\theta \equiv r (\cos \theta \cos \phi \gamma_1 + \cos \theta \sin \phi \gamma_2 - \sin \theta \gamma_3) \quad (7)$$

$$e_\phi \equiv r \sin \theta (-\sin \phi \gamma_1 + \cos \phi \gamma_2). \quad (8)$$

Note that e_θ and e_ϕ are not unit vectors and differ by factors r and $r \sin \theta$ from the usual spherical-polar basis vectors, respectively. This is a direct consequence of their definition in terms of the $\{\gamma_\mu\}$ frame (see Lasenby et al. 1998).

The translation and rotation gauge fields corresponding to the Boyer-Lindquist metric (1) are given in Doran, Lasenby & Gull (1996).

We start by defining an observer with covariant 4-velocity equal to γ_0 . Hereafter this observer will be called the γ_0 -observer. One can show that, at infinity, the γ_0 -observer is in a flat Minkowski space-time and at rest with respect to the central black hole. Elsewhere its function is to provide a useful frame in which to express quantities. In order to parameterise the energy and direction of the photon path, let us define the photon 4-momentum p in the $\{\gamma_\mu\}$ frame by

$$p = \Phi \gamma_0 + \Phi \sin \theta_p \cos \phi_p \gamma_1 + \Phi \sin \theta_p \sin \phi_p \gamma_2 + \Phi \cos \theta_p \gamma_3. \quad (9)$$

The photon energy as measured by the γ_0 -observer is given by $p \cdot \gamma_0$ which, from equation (9), is equal to Φ . Similarly, as illustrated in Fig. 1, the angles θ_p and ϕ_p correspond to the usual spherical-polar angles in the local spatial frame of the γ_0 -observer and define the direction at which photons are received (or emitted) by the γ_0 -observer. We note that p is guaranteed to be null since $p \cdot p = 0$, which is what is required for a massless particle. The photon trajectory itself is parameterised by the affine parameter λ . The spacetime position of the photon (t , r , θ , ϕ) is defined by the position vector

$$x = te_t + re_r, \quad (10)$$

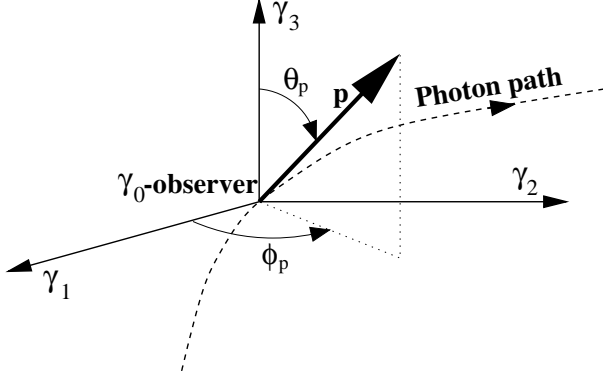


Figure 1. Photon 4-momentum p as measured by the γ_0 -observer. θ_p and ϕ_p are the observed angles of the photon trajectory.

where t , r , θ and ϕ are scalar functions of λ . The photon geodesic equations are given in Appendix B. The equations we obtain are all first order ordinary differential equations for t , r , θ , ϕ , Φ , θ_p and ϕ_p . As mentioned in the appendix, the attractive aspect of this approach is that the geodesic equations have been obtained without making use of conserved quantities along the photon path such as the energy, angular momentum or Carter constant. Instead these quantities can be used *a posteriori* as an effective check of both analytical and numerical results (see Appendix B).

2.2 Accretion Disc

We now employ a similar method as in Section 2.1 to study the properties of an accretion disc rotating around a Kerr black hole. In particular we are interested in the velocity and energy of the accreted material. The assumptions are the following:

(i) The accretion disc is a thin disc and lies in the equatorial plane ($\theta = \pi/2$), perpendicular to the axis of rotation of the central Kerr black hole.

(ii) The orbits are stable circular orbits. In the same way as we defined the photon momentum (9), we start here by defining the 4-velocity vector v_d of a particle in circular orbit of radius r around the black hole. Since the motion occurs in the equatorial plane, we can parameterise v_d as a function of γ_0 , γ_1 and γ_2 only:

$$v_d = \cosh U \gamma_0 + (\sinh U \cos \omega\tau) \gamma_1 + (\sinh U \sin \omega\tau) \gamma_2, \quad (11)$$

where ω represents the angular velocity and τ is the proper time along the world-line of the particle in circular orbit. U is a function of r , L and M , but not a function of τ since the orbit is circular. The parameterisation in \cosh and \sinh has been chosen to ensure that

$$v_d \cdot v_d = \cosh^2 U - \sinh^2 U = 1, \quad (12)$$

as required for a massive particle. In the $\{e_\mu\}$ frame, the velocity takes the simple form:

$$v_d = \cosh U e_t + \frac{\sinh U}{r} e_\phi. \quad (13)$$

We note that the γ_0 -observer is not comoving with the particle in orbit. Let us however assume that, at a given time t , the γ_0 -observer is at the position $(r, \theta = \pi/2, \phi)$, i.e.

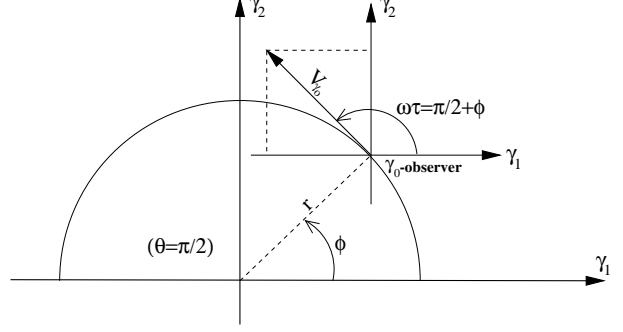


Figure 2. The 4-velocity of the orbiting particle, as measured by the γ_0 -observer at position $(r, \theta = \pi/2, \phi)$. $\omega\tau = \pi/2 + \phi$ and $V_{\gamma_0} = \tanh U$ are respectively the measured angle and magnitude of the velocity.

instantaneously at the same position as the orbiting particle (see Fig. 2). According to the γ_0 -observer, the energy per unit mass of the particle is given by $E_{\gamma_0} = v_d \cdot \gamma_0 = \cosh U$. The particle velocity has a magnitude $V_{\gamma_0} = \tanh U$ and makes an angle $\omega\tau = \pi/2 + \phi$ from the γ_1 axis in the local spatial frame $(\gamma_1, \gamma_2, \gamma_3)$ of the γ_0 -observer. When solving the dynamical equations, we find

$$\tanh U = \frac{-L \pm \sqrt{Mr}}{\Delta^{\frac{1}{2}}}, \quad (14)$$

and therefore

$$\begin{aligned} \cosh U &= \frac{\Delta^{\frac{1}{2}}}{\sqrt{r^2 - 3Mr \pm 2L\sqrt{Mr}}}, \\ \sinh U &= \frac{-L \pm \sqrt{Mr}}{\sqrt{r^2 - 3Mr \pm 2L\sqrt{Mr}}}. \end{aligned} \quad (15)$$

In the case where $L > 0$, the $+$ sign in (14) and (15) is for orbits co-rotating with the spinning hole, while the $-$ sign is for counter-rotating orbits. If $L < 0$ the significance of the signs is reversed.

Finally, following the same approach as in Appendix B, the conserved energy per unit mass E_r and angular momentum J_r of a circular orbit can be evaluated by using the Killing vectors K_t (equation B3) and K_ϕ (equation B4). We find

$$E_r = K_t \cdot v_d = E_{\gamma_0} \frac{r^2 - 2Mr \pm L\sqrt{Mr}}{r\Delta^{\frac{1}{2}}} \quad (16)$$

and

$$J_r = K_\phi \cdot v_d = E_{\gamma_0} \frac{L\Delta^{\frac{1}{2}} + L^2 V_{\gamma_0}}{r} + E_{\gamma_0} V_{\gamma_0} r. \quad (17)$$

The conserved quantity E_r in (16) is related to the local energy E_{γ_0} by a redshift factor, which tends to unity at infinity. Therefore E_r is usually called the *energy at infinity*. Regarding J_r in (17), the first term is a purely gravitational effect due to the dragging effect of the spinning hole, while the second term is more directly related to the Newtonian expression, mVr , of the angular momentum. We note that the condition for stability is given by $dE_r/dr > 0$, which gives the following condition for the minimum stable orbit r_{ms} :

$$\tanh U(r_{\text{ms}}) = \frac{1}{2}. \quad (18)$$

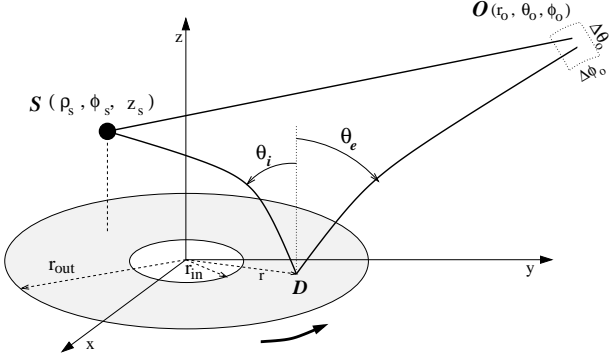


Figure 3. Geometrical set up of our Monte Carlo simulations. The spinning black hole is located at the centre of coordinates and the accretion disc lies on the equatorial plane from the inner radius r_{in} to the outer radius r_{out} . The arrow indicates the sense of rotation. The primary source is situated above the disc at an arbitrary position (ρ_s, ϕ_s, z_s) and illuminates both the disc and the collecting area of a distant observer located at (r_o, θ_o, ϕ_o) . The surface of the collecting area is $r_o^2 \sin \theta_o \Delta \phi_o \Delta \theta_o$.

It is perhaps somewhat surprising that the minimum stable orbit is for a local velocity of one half the speed of light. In this work, the accretion disc extends from $r = r_{\text{in}} = r_{\text{ms}}$ up to the arbitrary large outer radius $r = r_{\text{out}} = 5000 r_g$, where $r_g = GM/c^2$ is the gravitational radius.

2.3 Primary Source and Distant Observer

The primary X-ray source is assumed to be a *static* point source and, as shown in Fig. 3, is located above the disc at an arbitrary position (ρ_s, ϕ_s, z_s) , where ρ , ϕ and z are the usual cylindrical polar coordinates. The 4-velocity v_s of the source has to be proportional to the Killing vector K_t (equation B3) so that the source can remain static (see e.g. Misner et al. 1973). Requiring that $v_s \cdot v_s = 1$, we find

$$v_s = \frac{1}{\sqrt{1 - \frac{2Mr}{\rho^2}}} K_t \quad (19)$$

The source is emitting isotropically in its proper frame with a rate of emission defined by

$$N_{\nu_s} \propto \nu_s^\Gamma \text{ photon s}^{-1} \text{ Hz}^{-1}, \quad (20)$$

where Γ is the photon power-law index. Throughout this work we assume $\Gamma = -1.7$ (Mushotzky 1982; Turner & Pounds 1989).

Predictions regarding the iron line flux and equivalent width are those measured by a distant static observer. Since $K_t = \gamma_0$ for large r , the 4-velocity of the distant observer is

$$v_o = \gamma_0. \quad (21)$$

As illustrated in Fig. 3, the position of the distant observer is given by r_o, θ_o, ϕ_o with collecting area on the $r = r_o$ sphere equal to

$$\Delta A = r_o^2 \sin \theta_o \Delta \phi_o \Delta \theta_o. \quad (22)$$

2.4 Monte Carlo Simulations

The Monte Carlo simulations we carry out in this work have the advantage of computing both the continuum emission

and the reflected iron line flux as measured by a distant observer. In this manner the equivalent width of the line can be estimated in a consistent manner. A simulation consists of sending N photons from the source isotropically with respect to its proper frame. N_c of these photons will reach directly the observer's collecting area and therefore contribute to the continuum flux. N_l of them will be received after having hit the disc and being reprocessed into iron line photons. These contribute to the observed flux of the line. For each photon received on the collecting area, the total spectrum is computed by considering the total power in a succession of frequency bins of extent $\Delta\nu$. The following two sections (2.4.1 and 2.4.2) describe how the total power in each bin is estimated, first for the continuum emission then the reflected emission.

2.4.1 Continuum Emission

Let us consider a photon emitted by the source with 4-momentum p_s (equation 9) which reaches directly the collecting area at radius r_o with 4-momentum p_o . The redshift measured by the distant observer is therefore

$$1 + z_{so} = \frac{p_s \cdot v_s}{p_o \cdot v_o}, \quad (23)$$

Since $v_o = \gamma_0$ the denominator is simply the value of Φ at the observer, Φ_o . The numerator is calculated using (19) and (9). We find

$$1 + z_{so} = \frac{\Phi_s \left[\Delta^{\frac{1}{2}} - L \sin \theta \sin \theta_p \sin(\phi_p - \phi) \right]_s}{\Phi_o}, \quad (24)$$

where the subscript s indicates that the expression is evaluated at the source.

We define W_ν^c to be the continuum total power received in the collecting area of the distant observer in the range of frequency $[\nu, \nu + \Delta\nu]$. We have

$$W_\nu^c = \sum_{N_c} \int_\nu^{\nu+\Delta\nu} W_{\nu_o} d\nu_o, \quad (25)$$

where the sum is for each received continuum photon, W_{ν_o} is the received power per unit frequency attached to the photon, and the subscript o denotes quantities as measured by the distant observer. Expressing quantities on the right hand side of equation (25) in terms of quantities defined at the source, we obtain

$$W_\nu^c = \sum_{N_c} \left(\frac{1}{1 + z_{so}} \right)^2 \int_{\nu(1+z_{so})}^{(\nu+\Delta\nu)(1+z_{so})} \nu_s^{\Gamma+1} d\nu_s. \quad (26)$$

2.4.2 Reflected Iron Line

We now consider a photon that leaves the source with a 4-momentum p_s and hits the disc with a 4-momentum p_d . The redshift measured by the co-rotating observer is

$$1 + z_{sd} = \frac{p_s \cdot v_s}{p_d \cdot v_d}. \quad (27)$$

The numerator is given in (24) and the denominator can be calculated using (9) and (13). We find

$$1 + z_{sd} = \frac{\Phi_s \left[\Delta^{\frac{1}{2}} - L \sin \theta \sin \theta_p \sin(\phi_p - \phi) \right]_s}{\Phi_d \left[\cosh U - \sinh U \sin \theta_p \sin(\phi_p - \phi) \right]_d}, \quad (28)$$

where the subscripts s and d indicate that the expression is evaluated at the source and at the disc, respectively. A similar approach can be followed for the second part of the trajectory, from the disc to the collecting area of the distant observer. We find

$$1 + z_{do} = \frac{\Phi_d \left[\cosh U - \sinh U \sin \theta_p \sin(\phi_p - \phi) \right]_d}{\Phi_o}. \quad (29)$$

The radiation processes occurring on the disc are described in detail in George & Fabian (1991). Here, we are simplifying the situation significantly by ignoring the reflected continuum emission so that only the reflected iron line is taken into account (see Section 5 for a discussion of the validity of this approach). We define $N_{\nu_d}^{in}(\nu_d, \theta_i)$ to be the total number of photons impinging on the disc with energy ν_d and incidence angle θ_i per unit frequency and per unit time, as measured by a co-rotating observer (see Fig. 3). Following George & Fabian (1991), the number of fluorescent photons per unit frequency and per unit time which are able to escape the disc is

$$N_{\nu_d}^{out} = N_{\nu_d}^{in}(\nu_d, \theta_i) g(\theta_i) f(\nu_d), \quad (30)$$

where,

$$g(\theta_i) = (6.5 - 5.6 \cos \theta_i + 2.2 \cos^2 \theta_i) \times 10^{-2}, \quad (31)$$

$$f(\nu_d) = 7.4 \times 10^{-2} + 2.5 \exp\left(-\frac{\nu_d - 1.8}{5.7}\right). \quad (32)$$

This analytical approximation is valid for $\nu_t < \nu_d < \nu_m$, where $\nu_t = 7.1$ keV is the energy threshold for triggering the 6.4 keV iron fluorescent emission, and $\nu_m = 30$ keV. As given in Ghisellini, Haardt & Matt (1994), the intensity of the emerging fluorescent emission is not isotropic and is here assumed to be proportional to $\cos \theta_e \ln(1 + 1/\cos \theta_e)$, where θ_e is the outgoing inclination angle as measured in the co-rotating frame. Therefore $N_{\nu_d}^{out}$ follows the angular distribution

$$N_{\nu_d}^{out}(\theta_e) d\theta_e = 2 \cos \theta_e \ln\left(1 + \frac{1}{\cos \theta_e}\right) \sin \theta_e d\theta_e. \quad (33)$$

We now define W_ν^l to be the iron line total power received in the collecting area of the distant observer in the range of frequency $[\nu, \nu + \Delta\nu]$. Following a similar reasoning as in Section 2.4.1 we obtain

$$W_\nu^l = \sum_{N_i} \delta_\nu \left(\frac{1}{1 + z_{do}} \right)^2 N^{out} \nu_\alpha, \quad (34)$$

where $\nu_\alpha = 6.4$ keV, $\delta_\nu = 1$ if $\nu < \nu_\alpha/(1 + z_{do}) < \nu + \Delta\nu$, $\delta_\nu = 0$ otherwise, and

$$N^{out} = g(\theta_i) \int_{\nu_t}^{\nu_m} f(\nu_d) N_{\nu_d}^{in} d\nu_d. \quad (35)$$

When expressed in the source proper frame, we have

$$W_\nu^l = \sum_{N_i} \delta_\nu \left(\frac{1}{1 + z_{do}} \right)^2 \frac{1}{1 + z_{sd}} \nu_\alpha g(\theta_i) \times \int_{\nu_t(1+z_{sd})}^{\nu_m(1+z_{sd})} f\left(\frac{\nu_s}{1+z_{sd}}\right) \nu_s^\Gamma d\nu_s. \quad (36)$$

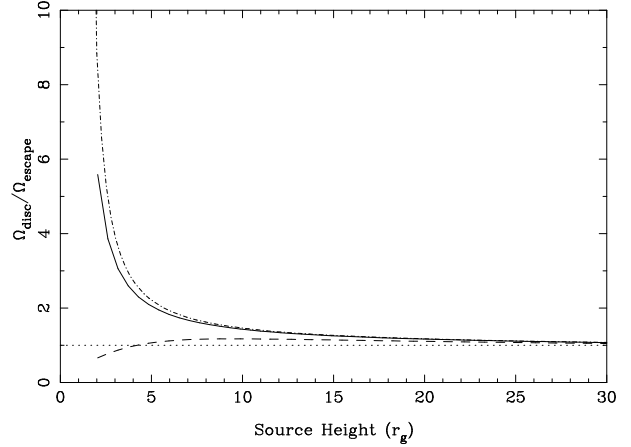


Figure 4. Ratio of the solid angle formed by the rays hitting the disc to the solid angle formed by rays escaping to infinity. The solid line is for a maximally rotating Kerr black hole while the dashed curve is for a Schwarzschild hole. The dotted-dashed curve is for the ratio of solid angle formed by rays deflected towards the equatorial plane, including those lensed towards the event horizon. The dotted line indicates the ratio that would be obtained without the gravitational bending effect.

3 SOURCE ON AXIS

When discussing the fluorescent iron line profile and equivalent width, many authors have considered the situation where the primary X-ray source is located above the disc, on the axis of rotation (e.g. Martocchia et al. 1999, Matt et al. 1992, Martocchia & Matt 1996; Reynolds & Begelman 1997, Young, Ross & Fabian 1998; Reynolds et al. 1999). This assumption has the advantage of simplifying both calculations and analysis since the axial symmetry of the problem is conserved. In this section we also follow this assumption, but it will be relaxed in Section 4.

3.1 Gravitational Lensing Effect

As pointed out by Martocchia & Matt (1996), if the primary source is very close to the hole, a significant fraction of the primary photon rays will be lensed towards the disc, decreasing considerably the direct flux relatively to the reflected flux, as observed by a distant observer. In order to quantify this phenomena, the ratio of the solid angle formed by the rays hitting the disc to the solid angle formed by the rays escaping to infinity ($\Omega_{\text{disc}}/\Omega_{\text{escape}}$) is plotted versus the height $h = z_s$ of the source in Fig. 4. The effect is negligible in the case of a Schwarzschild black hole since a large amount of the lensed radiation is lost within the innermost stable orbit of the disc (i.e. $6 r_g$). In the case of a maximally rotating Kerr black hole, where the inner radius of the disc can be as small as $1 r_g$, the effect becomes significant for a sufficiently close source, typically $h < 6 r_g$ as seen on Fig. 4. However, in the case of a source at height $h = 2 r_g$, Ω_{disc} is only a factor of ~ 5.5 bigger than Ω_{escape} . In this case we find that almost half of the rays bent towards the equatorial plane do not actually hit the disc but are strongly lensed towards the event horizon, resulting in a significant damping of the effect.

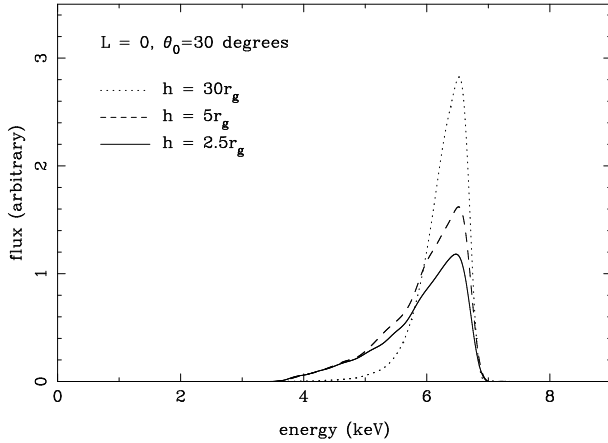


Figure 5. Predicted spectral line shapes for a central Schwarzschild black hole ($L = 0$), as seen by a distant observer at inclination angle $\theta_0 = 30$ degrees. The primary source is located on the axis of rotation at height h from the origin. The solid, dashed and dotted lines are for $h = 2.5, 5$ and $30r_g$ respectively. The area under each curve is proportional to the line equivalent width.

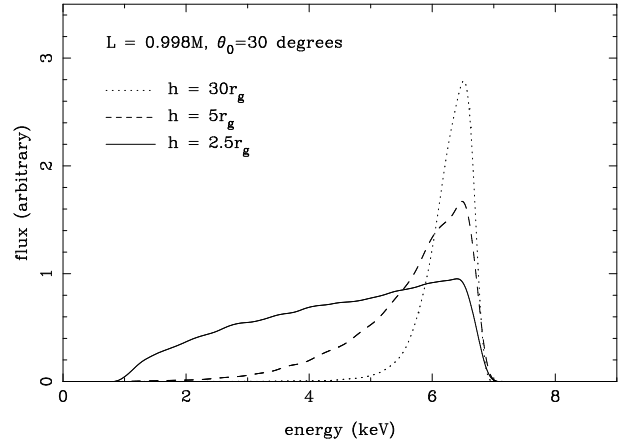


Figure 7. Predicted spectral line shapes for a maximally rotating Kerr black hole ($L = 0.998M$), as seen by a distant observer at inclination angle $\theta_0 = 30$ degrees. The primary source is located on the axis of rotation at height h from the origin. The solid, dashed and dotted lines are for $h = 1.5, 5$ and $30r_g$ respectively. The area under each curve is proportional to the line equivalent width.

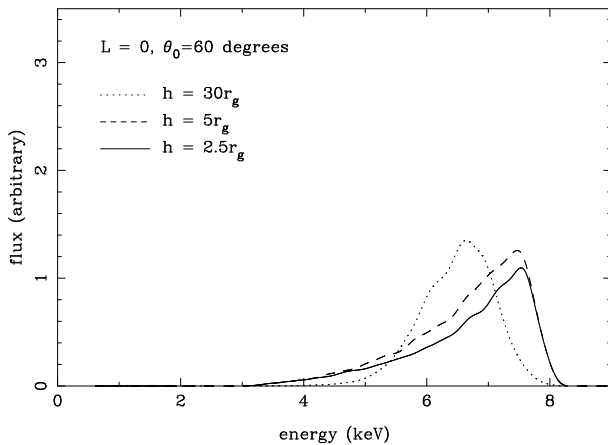


Figure 6. Same as Fig. 5 but for $\theta_0 = 60$ degrees.

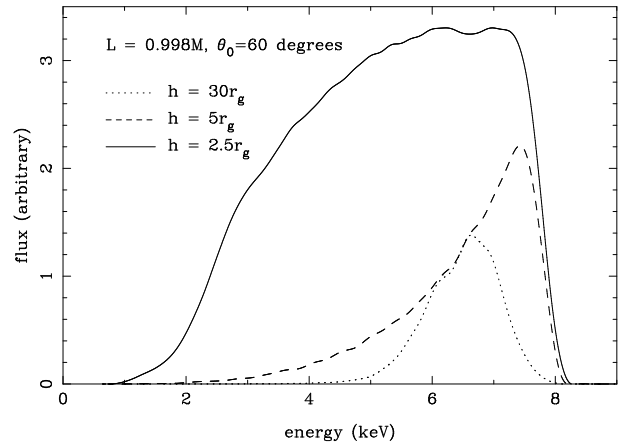


Figure 8. Same as Fig. 7 but for $\theta_0 = 60$ degrees.

3.2 Line Profiles

Examples of line profiles obtained with our Monte-Carlo simulations for various values of h are given in Figs. 5, 6, 7 and 8 for the maximum Kerr and the Schwarzschild cases. The predicted line shapes are for distant observers at inclination angles $\theta_0 = 30$ degrees and $\theta_0 = 60$ degrees. As already noticed in previous studies (e.g. Fabian et al. 1989, Dabrowski et al. 1997), the line extends further towards the blue shifted part of the spectrum for larger inclination angles. Indeed, for large θ_0 the blue part of the line is boosted by the Doppler effect due to the rotation of the disc. On the other hand, the extension towards the red shifted part of the spectrum is controlled by the strength of the gravitational redshift which increases as the fluorescent emission happens closer to the central black hole. This is very clearly illustrated here for the maximally rotating Kerr case (Figs 7, 8), where ν/ν_α could be as small as 0.16 for a source located at $h = 1.5 r_g$. Indeed, as the source gets closer to the hole it illuminates more intensively the inner part of the disc, resulting in strong gravitational redshift of the fluorescent

line. In the Schwarzschild case as well (Figs. 5, 6) the reddening of the line increases as the source gets closer to the hole. However, because the inner radius of the disc is $6 r_g$ as opposed to $1.24 r_g$ in the maximally rotating Kerr case, less strong reddening is predicted in the Schwarzschild case. For example, one can notice very little difference between the predicted lines for $h = 5 r_g$ and $h = 2.5 r_g$. In particular the red wing is not more extended in the $h = 2.5 r_g$ case because most of the illumination is focused within the minimum stable orbit.

3.3 Equivalent Width

The equivalent width (EW) of the iron fluorescent line is estimated as follows:

$$EW = \frac{\int_0^\infty W_\nu^l d\nu}{W_{\nu=\nu_\alpha}^c}. \quad (37)$$

Results are given in Figs. 9 and 10 as a function of the height of the primary source in the maximally rotating Kerr case ($L = 0.998M$), in the Schwarzschild case ($L = 0$) and in an

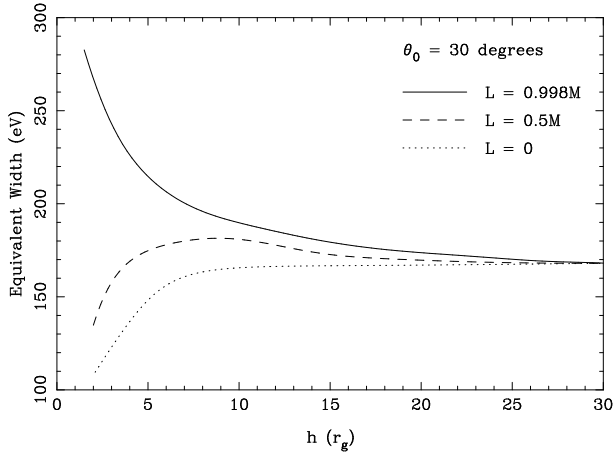


Figure 9. Equivalent width of the iron fluorescent line as a function of the height h of the source. The solid, dashed, and dotted lines are for $L = 0.998M$, $L = 0.5M$ and $L = 0$ respectively. The distant observer is at inclination $\theta_0 = 30$ degrees.

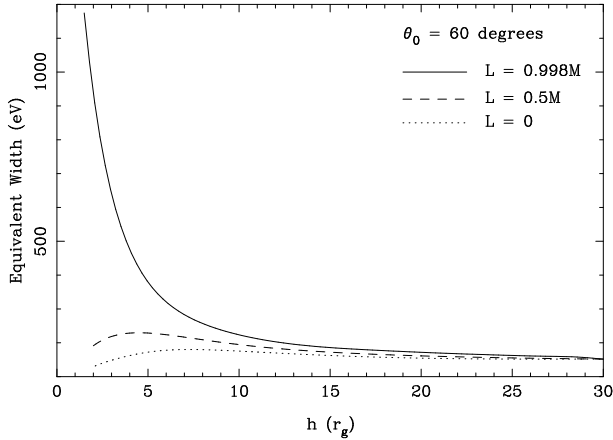


Figure 10. Same as Fig.9 but for an observer at inclination $\theta_0 = 60$ degrees.

intermediate case where $L = 0.5M$. Fig. 9 is for a distant observer with inclination $\theta_0 = 30$ degrees and Fig. 10 is for $\theta_0 = 60$ degrees. We expect the strength of the line to be larger as the source gets closer to the hole since the primary emission would preferentially be focused towards the plane of the disc. This effect is clearly visible in the case of a maximally rotating Kerr black hole (solid lines in Figs.9 & 10). However, for lower values of the black hole spin and consequently higher values of the inner radius of the disc, this EW enhancement effect is lessened, as predicted in Section 3.1. In cases where the source is so close to the hole that most of the lensed illumination is lost within the inner radius of the disc, the effect is actually reversed and the EW diminishes as the primary source gets closer to the hole. In particular, no EW enhancement is predicted in the case of a Schwarzschild black hole. For a distant observer at inclination $\theta_0 = 30$ degrees the maximum EW is predicted to be ~ 290 eV, while the EW obtained for the *classical* case where no lensing effect comes into play (i.e. large h) is ~ 165 eV. Therefore, even for a primary source located just above the event horizon of a maximally rotating Kerr black hole, the EW enhancement is less than a factor of two. As seen in

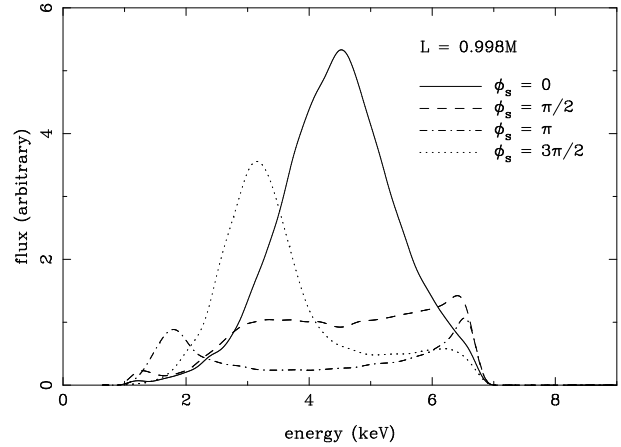


Figure 11. Predicted spectral line shapes for a maximally rotating black hole ($L = 0.998M$), as seen by a distant observer at inclination angle $\theta_0 = 30$ degrees and azimuthal angle $\phi_o = \pi/2$. The primary sources are located at $\rho_s = 2.5 r_g$ and $z_s = 1 r_g$, in each case. The solid, dashed, dashed-dot and dotted lines are for $\phi_s = 0$, $\phi_s = \pi/2$, $\phi_s = \pi$ and $\phi_s = 3\pi/2$ respectively. The area under each curve is proportional to the line equivalent width.

Fig.10, the gravitational lensing effect becomes more effective when observed from a large inclination angle. Indeed, the line is strengthened by the lensing effect for both low and high inclination angle points of view. However, due to the same effect, the continuum emission received at large θ_0 is strongly reduced compared to that received at smaller θ_0 . For an observer at inclination $\theta_0 = 60$ degrees, EWs as high as ~ 1.2 keV are predicted, which represents an EW enhancement factor of about 8. This strong EW enhancement effect can also be seen in Fig. 8, where the area under each line is proportional to the line EW. However in the case of MCG-6-30-15 the disc is thought to have a inclination angle of about 30 degrees (e.g. Tanaka et al. 1995; Dabrowski et al. 1997).

4 SOURCE OFF AXIS

We have seen in Section 3 that the EW enhancement is limited by the fact that a significant proportion of the primary illumination is ‘lost’ within the inner radius of the disc instead of contributing to the strengthen of the iron line. This limiting effect is particularly important when the primary source lies above the disc on the axis of rotation. Stronger EW enhancement should be obtained by relaxing this assumption and allowing the primary source not to lie right above the event horizon of the hole. In this section, we investigate this possibility in the maximally rotating Kerr solution ($L = 0.998M$).

Since the axial symmetry of the system is here broken, we need to define the distant observer by both the inclination θ_0 and the azimuthal angle ϕ_o . For simplicity, here we fix the observer at $\phi_o = \pi/2$ while allowing the source to be located at various azimuths ϕ_s above the disc, as suggested in Fig. 3. Line spectra are given in Fig. 11 as a function of ϕ_s for sources located at height $z_s = 1 r_g$ above the plane of the disc and radius $\rho_s = 2.5 r_g$ from the axis of rotation, close to the ergosphere radius at this latitude ($1.93 r_g$). Since the illumination takes place above the inner parts of the disc,

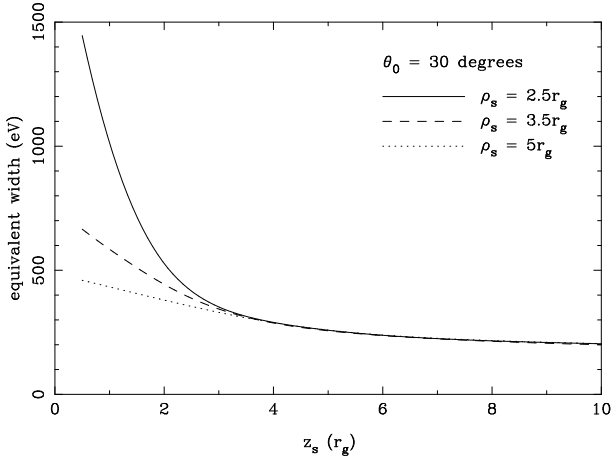


Figure 12. Equivalent width of the iron fluorescent line as a function of the height z_s of the source. The primary source is at azimuth $\phi_s = 0$, above the approaching side of the disc. The solid, dashed and dotted lines are for $\rho_s = 2.5$, 3.5 and $5 r_g$ respectively. The central black hole is a maximally rotating black hole ($L = 0.998M$) and the distant observer is at inclination $\theta_o=30$ degrees and azimuth $\phi_o = \pi$.

all these lines display strongly redshifted features. However, as one can notice on Fig. 11, the shape of the spectral line varies significantly as a function of ϕ_s . For $\phi_s = 0$ the line is mostly redshifted and its flux peaks at around 4.5 keV, while for $\phi_s = \pi$ the line is double peaked around 1.8 keV and 6.5 keV. In the former case the primary source is located above the approaching part of the disc where the emission is significantly boosted by the Doppler effect. In the latter case, the strongly redshifted red wing is the result of Doppler shift from the receding part of the disc, while the blue wing is due to rays that have reached the approaching side of the disc while spiralling down on to the disc. Lines for $\phi_s = \pi/2$ and $\phi_s = 3\pi/2$ are hybrids of the above two cases.

Since the illumination occurs right above the Doppler boosted region of the disc for $\phi_s = 0$, the predicted line EW is much larger in this geometrical situation than for other values of ϕ_s . This is illustrated in Fig. 11 where the spectral line integrals are proportional to their EW. For the rest of this section we assume that the primary source is always located at this privileged azimuthal angle $\phi_s = 0$. Figs. 12 and 13 give the predicted iron line EW as a function of the primary source height z_s and radius ρ_s . In the case of an observer at inclination $\theta_o=30$ degrees, the observed EW can be much larger than for a source located on the axis of rotation. For example, as seen on Fig.12, for a primary source located at ($\rho_s = 2.5 r_g$, $\phi_s = 0$, $z_s = 1 r_g$) the predicted EW is ~ 1 keV and if the source is as close as $z_s = 0.5 r_g$ to the disc the EW can be as high as ~ 1.5 keV. In this latter case, the EW is enhanced by a factor of ~ 10 of its *classical* value. However, in order to reach such high EW the primary source needs to be located above the very inner parts of the disc. For example, in the case of a source located at ($\rho_s = 5 r_g$, $\phi_s = 0$, $z_s = 0.5 r_g$) the predicted line EW is only ~ 500 eV. As a consequence, very little EW enhancement is expected in the case of slowly rotating black holes. As expected, for an observer at inclination $\theta_o=60$ degrees the predicted line EW is much larger than for $\theta_o=30$ degrees. As seen on Fig.13, in the extreme case where the primary source is located at

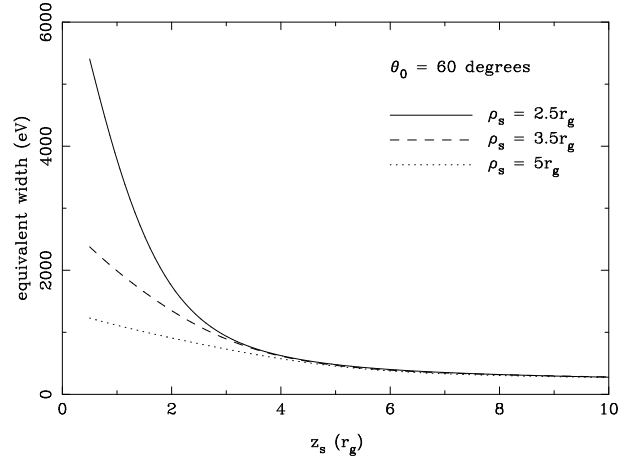


Figure 13. Same as Fig. 12 but for an observer at inclination $\theta_o=60$ degrees.

($\rho_s = 2.5 r_g$, $\phi_s = 0$, $z_s = 0.5 r_g$), the observed EW can be as high as ~ 5.5 keV, which represents an EW enhancement factor of about 35.

5 DISCUSSION

In Section 2 we have presented a new fully relativistic approach to calculating photon paths and energies in the Boyer-Lindquist metric. The geodesic equations obtained in this approach are simple first order ordinary differential equations which allow easy and stable numerical integration. Furthermore, the way the photon 4-momentum is parameterised (equation 9) allows us to be very clear regarding observable quantities such as the frequency and incoming/outgoing angles of the light ray, as measured by an observer. We believe that our theoretical approach is an improvement compared to more standard methods usually employed in similar applications (e.g. Reynolds et al. 1999).

We found in Sections 3 and 4 that large values of the observed iron line equivalent width (EW) may be explained by general relativistic effects when the primary X-ray source lies above the very inner part of an accretion disc (within ~ 5 gravitational radii) around a maximally rotating central black hole. When the primary source is located on the axis of rotation, EWs up to ~ 300 eV only can be accounted for by this model for a disc at inclination 30 degrees. This is a much lower prediction than that of the early work of Martocchia & Matt (1996) who found EWs up to ~ 1500 eV for a comparable case. Our results are however in good agreement with the very recent work of Martocchia et al. (1999). At inclination 60 degrees EWs up to ~ 1.2 keV are predicted.

By allowing the primary source to be located off the axis of rotation, we found that much larger values of the EW are obtained when the source is located above the approaching side of the disc (up to ~ 1.5 keV and ~ 5.5 keV for inclination 30 and 60 degrees respectively). However, in the most extreme cases, a reflected continuum component should also be included in the model, in addition to the reflected iron line (Lightman & White 1988; Pounds et al. 1990; Matt et al. 1991; George & Fabian 1991). When the reflected emission is not enhanced by the lensing of the primary light rays, the reflected continuum accounts for about 10 percent of

the observed continuum flux at 6.4 keV. One would therefore expect the reflected continuum to dominate when the enhancement factor reaches ~ 10 . Beyond this value, the continuum flux observed at 6.4 keV increases together with the iron line flux and therefore the line should no longer gain in strength. As a result one should regard values of Fig. 13 as indicative of the strength of the lensing enhancement effect, while the actual observed iron line EW should not be larger than ~ 1600 eV (i.e. 10 times its *classical* value).

Results found in Section 4 may be used as arguments towards explaining the large iron line EW observed in Seyfert-1 galaxies. Such an explanation may be valid for the EW enhancement observed in the case of MCG-6-30-15 where it is likely that strong emission processes take place very close to the hole, at least during specific periods (see Iwasawa et al. 1996, 1999). However, as highlighted by Reynolds & Fabian (1997), in the case of more typical objects it is less probable that strong emission would occur so close to the hole. Reynolds & Fabian (1997) found that the relative motion between the disc and the source may significantly affect the EW of the line, simply by special relativistic arguments. This could allow EW enhancement even when the emission occurs further away from the hole. Such an effect could be investigated in our model by allowing the source to have a peculiar velocity. For example, a simple model where the source moves with a constant angular velocity could be assumed (Yu & Lu 1999).

ACKNOWLEDGEMENTS

YD would like to thank Trinity Hall, Cambridge for support in the form of a Research Fellowship. The authors also thank Andy Fabian and Anthony Challinor for useful discussions.

REFERENCES

- Blandford R., Rees M.J., 1992, in *Testing the AGN Paradigm*, Holt S.N. and Urry C., editors, AIP Conference 254 (1991), p. 3, American Institute of Physics.
- Bromley B.C., Chen K., Miller W.A., 1997, ApJ, 475, 57
- Cadez A., Fanton C., Calvani M., 1998, New Astronomy, 3, 647
- Dabrowski Y., 1998, in *Strong Gravitational Phenomena in Active Galactic Nuclei and the Cosmic Microwave Background*, Ph.D. thesis, Cambridge University, UK
- Dabrowski Y., Fabian A.C., Iwasawa K., Lasenby A.N., Reynolds C.S., 1997, MNRAS, 288, L11
- D’Inverno R., 1992, in *Introduction Einstein’s Relativity*, Oxford University Press, UK.
- Doran C.J.L., Lasenby A.N., Gull S.F., 1996, in Baylis W., editor, *Clifford (Geometric) Algebras*, p. 211, Birkhauser, Boston.
- Fabian A.C., Rees M.J., Stella L., White N.E., MNRAS, 238, 1989
- George I.M., Fabian A.C., 1991, MNRAS, 249, 352
- Ghisellini G., Haardt F., Matt G., 1994, MNRAS, 267, 743
- Hestenes D., 1966, in *Space-Time Algebra*, Gordon and Breach, New York.
- Iwasawa K., Fabian A.C., Reynolds C.S., Nandra K., Otani C., Inoue H., Hayashida K., Brandt W.N., Dotani T., Kunieda H., Matsuoka M., Tanaka Y., 1996, MNRAS, 282, 1038
- Iwasawa K., Fabian A.C., Young A.J., Inoue H., Matsumoto C., 1999, MNRAS, 306, L19
- Lasenby A.N., Doran C., Gull S.F., 1998, Phil. Tran. R. Soc. Lond. A, 356, 487

- Lee J.C., Fabian A.C., Reynolds C.S., Iwasawa K., Brandt W.N., 1998, MNRAS, 300, 583
- Lee J.C., Fabian A.C., Brandt W.N., Reynolds C.S., Iwasawa K., 1999, MNRAS, in press
- Lightman A.P., White T.R., 1988, ApJ, 335, 57
- Matt G., Perola G.C., Piro L., 1991, A&A, 247, 25
- Matt G., Perola G.C., Piro L., Stella L., 1992, A&A, 257, 63
- Martocchia A., Matt G., 1996, MNRAS, 282, L53
- Martocchia A., Karas V., Matt G., 1999, MNRAS, in press
- Matsuoka M., Piro L., Yamauchi M., Murakami T., 1990, ApJ, 361, 440
- Misner C.W., Thorne K.S., Wheeler J.A., 1973, in *Gravitation*, W.H. Freeman and Company, New York.
- Mushotzky R.F., 1982, ApJ, 256, 92
- Nandra K., Pounds K.A., Stewart G.C., Fabian A.C., Rees M.J., 1989, MNRAS, 236, 39
- Nandra K., George I.M., Mushotzky R.F., Turner T.J., Yaqoob T., 1997, ApJ, 477, 602
- Pounds K.A., Nandra K., Stewart G.C., Leighly K., 1989, MNRAS, 240, 769
- Pounds K.A., Nandra K., Stewart G.C., George I.M., Fabian A.C., 1990, Nat, 344, 132
- Rees M.J., 1984, A&AR, 22, 471
- Reynolds C.S., Begelman M.C., 1997, ApJ, 488, 109
- Reynolds C.S., Fabian A.C., 1997, MNRAS, 290, L1
- Reynolds C.S., Young A.J., Begelman M.C., Fabian A.C., 1999, ApJ, 514, 164
- Tanaka Y., Nandra K., Fabian A., Inoue H., Otani C., Dotani T., Hayashida K., Iwasawa K., Kii T., Kunieda H., Makino F., Matsuoka M., 1995, Nat, 375, 659
- Turner T.J., Pounds K.A., 1989, MNRAS, 240, 833
- Young A.J., Ross R.R., Fabian A.C., 1998, MNRAS, 300, L11
- Yu Q., Lu Y., 1999, MNRAS, in press

APPENDIX A: GENERAL RELATIVISTIC APPROACH

This work has been carried out using the gauge-theoretic formalism described in detail in Lasenby et al. (1998). However, the theoretical calculations presented in Section 2 and Appendix B could in principle be carried out following a more standard general relativistic approach by making use of orthogonal tetrads (see e.g. Misner et al. 1973). A suitable tetrad frame in the Boyer-Lindquist metric (equation 1) can be defined as follows:

$$(e_t)^\mu = \left(\frac{r^2 + L^2}{\rho \Delta^{\frac{1}{2}}}, 0, 0, \frac{L}{\rho \Delta^{\frac{1}{2}}} \right) \quad (\text{A1})$$

$$(e_r)^\mu = \left(0, \frac{\Delta^{\frac{1}{2}}}{\rho}, 0, 0 \right) \quad (\text{A2})$$

$$(e_\theta)^\mu = \left(0, 0, \frac{r}{\rho}, 0 \right) \quad (\text{A3})$$

$$(e_\phi)^\mu = \left(\frac{Lr \sin^2 \theta}{\rho}, 0, 0, \frac{r}{\rho} \right), \quad (\text{A4})$$

where $\mu = 0 \dots 3$ are the usual coordinate indexes, corresponding here to the Boyer-Lindquist coordinates (t, r, θ, ϕ) . This tetrad can be identified with the coordinate frame $\{e_\mu\}$ defined by equations (5) to (8). The orthonormal tetrad corresponding to the $\{\gamma_\mu\}$ frame (equation 4) is given by

$$(\gamma_0)^\mu = \left(\frac{r^2 + L^2}{\rho \Delta^{\frac{1}{2}}}, 0, 0, \frac{L}{\rho \Delta^{\frac{1}{2}}} \right) \quad (\text{A5})$$

$$(\gamma_1)^\mu = \left(\frac{-L \sin \theta \sin \phi}{\rho}, \frac{\Delta^{\frac{1}{2}} \sin \theta \cos \phi}{\rho}, \frac{\cos \theta \cos \phi}{\rho}, \frac{-\sin \phi}{\rho \sin \theta} \right) \quad (\text{A6})$$

$$(\gamma_2)^\mu = \left(\frac{L \sin \theta \cos \phi}{\rho}, \frac{\Delta^{\frac{1}{2}} \sin \theta \sin \phi}{\rho}, \frac{\cos \theta \sin \phi}{\rho}, \frac{\cos \phi}{\rho \sin \theta} \right) \quad (\text{A7})$$

$$(\gamma_3)^\mu = \left(0, \frac{\Delta^{\frac{1}{2}} \cos \theta}{\rho}, \frac{-\sin \theta}{\rho}, 0 \right). \quad (\text{A8})$$

The equations given in Section 2 can now be translated into this general relativistic context. For example equation (9) of Section 2.1 should be read as follows

$$p^\mu = \Phi (\gamma_0)^\mu + \Phi \sin \theta_p \cos \phi_p (\gamma_1)^\mu + \Phi \sin \theta_p \sin \phi_p (\gamma_2)^\mu + \Phi \cos \theta_p (\gamma_3)^\mu. \quad (\text{A9})$$

While the photon geodesic equations \dot{t} , \dot{r} , $\dot{\theta}$, $\dot{\phi}$ given in Appendix B are obtained by the following equation

$$p^\mu = \frac{(dx)^\mu}{d\lambda}, \quad (\text{A10})$$

where

$$(dx)^\mu = (dt, dr, d\theta, d\phi). \quad (\text{A11})$$

APPENDIX B: PHOTON GEODESIC EQUATIONS

When solving the geodesic equations in the Boyer-Lindquist metric for the photon 4-momentum given in Section 2.1 (see Lasenby et al. 1998), we find

$$\begin{aligned}
 \frac{dt}{d\lambda} &= \frac{\Phi}{\rho\Delta^{\frac{1}{2}}} \left[L^2 + r^2 + L\Delta^{\frac{1}{2}} \sin\theta \sin\theta_p \sin(\phi_p - \phi) \right], \\
 \frac{dr}{d\lambda} &= \frac{\Phi\Delta^{\frac{1}{2}}}{\rho} \left[\cos\theta_p \cos\theta + \sin\theta \sin\theta_p \cos(\phi_p - \phi) \right], \\
 \frac{d\theta}{d\lambda} &= \frac{\Phi}{\rho} \left[\cos\theta \sin\theta_p \cos(\phi_p - \phi) - \sin\theta \cos\theta_p \right], \\
 \frac{d\phi}{d\lambda} &= \frac{\Phi}{\rho\Delta^{\frac{1}{2}} \sin\theta} \left[\Delta^{\frac{1}{2}} \sin\theta_p \sin(\phi_p - \phi) + L \sin\theta \right],
 \end{aligned} \tag{B1}$$

and for the photon 4-momentum

$$\begin{aligned}
 \frac{d\Phi}{d\lambda} &= \frac{\Phi^2}{\rho^3} \left\{ \left[\cos\theta \cos\theta_p + \sin\theta \sin\theta_p \cos(\phi_p - \phi) \right] (2\rho^2 - r^2 - r\Delta^{\frac{1}{2}} + B) - L^2 \cos\theta \cos\theta_p \right\}, \\
 \frac{d\phi_p}{d\lambda} &= \frac{\Phi}{\rho^3} \left\{ -B \frac{\sin(\phi_p - \phi) \sin\theta}{\sin\theta_p} + LA \left[\frac{\cos(\phi_p - \phi) \sin 2\theta}{2 \tan\theta_p} - \cos^2\theta \right] + L\rho^2 \Delta^{-\frac{1}{2}} \right\}, \\
 \frac{d\theta_p}{d\lambda} &= \frac{\Phi \cos\theta}{\rho^3} \left\{ B \left[\tan\theta \cos(\phi_p - \phi) \cos\theta_p - \sin\theta_p \right] + LA \sin\theta \sin(\phi_p - \phi) \right\},
 \end{aligned} \tag{B2}$$

where

$$\begin{aligned}
 A &= 2L \sin\theta_p \sin(\phi_p - \phi) \sin\theta + 2\Delta^{\frac{1}{2}}, \\
 B &= Ar + \rho^2 \Delta^{-\frac{1}{2}} \left(M - r - \Delta^{\frac{1}{2}} \right).
 \end{aligned}$$

We note the very simple form of the ordinary first order differential equations obtained for \dot{t} , \dot{r} , $\dot{\theta}$ and $\dot{\phi}$, where overdots denote differentiation with respect to λ . The $\dot{\Phi}$, $\dot{\theta}_p$ and $\dot{\phi}_p$ expressions are slightly more complex but still are first order ordinary differential equations. This approach is therefore useful because of the computational advantage of first order equations in terms of efficiency and stability.

An interesting aspect of the geodesic equations (B1) and (B2) is that they do not rely on conserved quantities such as the energy, angular momentum or Carter constant along the photon path. As a consequence, one can actually compute these quantities and verify that they are indeed conserved along the trajectory. This allows one to check easily the analytical expressions (B1) and (B2) as well as the corresponding numerical code. The conserved energy E_p and angular momentum J_p of a photon geodesic are evaluated by making use of the Killing vectors K_t and K_ϕ associated with the temporal and axial symmetries of (1) respectively. We have

$$K_t = \frac{\Delta^{\frac{1}{2}}}{\rho} e_t - \frac{L}{\rho r} e_\phi. \tag{B3}$$

and

$$K_\phi = -\frac{L\Delta^{\frac{1}{2}} \sin^2\theta}{\rho} e_t + \frac{r^2 + L^2}{\rho r} e_\phi. \tag{B4}$$

Therefore

$$E_p = p \cdot K_t = \Phi \left[\frac{L \sin\theta \sin\theta_p \sin(\phi_p - \phi) + \Delta^{\frac{1}{2}}}{\rho} \right] \tag{B5}$$

and

$$J_p = p \cdot K_\phi = -\Phi \sin\theta \left[\frac{(L^2 + r^2) \sin\theta_p \sin(\phi_p - \phi) + L\Delta^{\frac{1}{2}} \sin\theta}{\rho} \right] \tag{B6}$$

The derivatives \dot{E}_p and \dot{J}_p with respect to the affine parameter λ can be obtained. As expected, substituting for the expressions of \dot{r} , $\dot{\theta}$, $\dot{\phi}$, $\dot{\Phi}$, $\dot{\theta}_p$ and $\dot{\phi}_p$ found above leads to

$$\frac{dE_p}{d\lambda} = \frac{dJ_p}{d\lambda} = 0. \tag{B7}$$

This paper has been produced using the Royal Astronomical Society/Blackwell Science L^AT_EX style file.